



Article

Tomographic Imaging of Ionospheric Plasma Bubbles Based on GNSS and Radio Occultation Measurements

Fabricio dos Santos Prol^{1,2,*}, Manuel Hernández-Pajares^{2,3},
Marcio Tadeu de Assis Honorato Muella⁴ and Paulo de Oliveira Camargo¹

¹ Department of Cartography, Universidade Estadual Paulista (UNESP), Presidente Prudente 19060-900, São Paulo, Brazil; paulo.camargo@unesp.br

² Department of Mathematics, Universitat Politècnica de Catalunya—IONospheric determination and Navigation based on Satellite and Terrestrial systems (UPC-IonSAT), E08034 Barcelona, Spain; manuel.hernandez@upc.edu

³ Institut d'Estudis Espacials de Catalunya—Grup de Recerca en Ciències i Tecnologies de l'Espai (IEEC-CRAE-CTE), Universitat Politècnica de Catalunya (UPC), E08034 Barcelona, Spain

⁴ Laboratory of Physics and Astronomy, Institute of Research and Development (IP&D), Universidade do Vale do Paraíba (UNIVAP), São José dos Campos 12244-000, Brazil; mmuella@univap.br

* Correspondence: fabricioprol@hotmail.com; Tel.: +55-18-3229-5414

Received: 1 August 2018; Accepted: 12 September 2018; Published: 23 September 2018



Abstract: Total electron content measurements given by the global navigation satellite system (GNSS) have successfully presented results to capture the signatures of equatorial plasma bubbles. In contrast, the correct reproduction of plasma depletions at electron density level is still a relevant challenge for ionospheric tomographic imaging. In this regard, this work shows the first results of a new tomographic reconstruction technique based on GNSS and radio-occultation data to map the vertical and horizontal distributions of ionospheric plasma bubbles in one of the most challenging conditions of the equatorial region. Twenty-three days from 2013 and 2014 with clear evidence of plasma bubble structures propagating through the Brazilian region were analyzed and compared with simultaneous observations of all-sky images in the 630.0 nm emission line of the atomic oxygen. The mean rate of success of the tomographic method was 37.1%, being more efficient near the magnetic equator, where the dimensions of the structures are larger. Despite some shortcomings of the reconstruction technique, mainly associated with ionospheric scintillations and the weak geometry of the ground-based GNSS receivers, both vertical and horizontal distributions were mapped over more than 30° in latitude, and have been detected in instances where the meteorological conditions disrupted the possibility of analyzing the OI 630 nm emissions. Therefore, the results revealed the proposed tomographic reconstruction as an efficient tool for mapping characteristics of the plasma bubble structures, which may have a special interest in Space Weather, Spatial Geodesy, and Telecommunications.

Keywords: equatorial ionosphere; plasma bubble detection; total electron content mapping; multiplicative algebraic reconstruction technique; optical imaging; 630.0 nm emission line

1. Introduction

Ionospheric plasma bubbles are large-scale structures of density depletion in the Earth's ionosphere. It is well known that the plasma bubbles are generated by plasma instability mechanisms in the lower F region, and grow aligned with the magnetic field up to ~1500 km over the equatorial region [1]. Typical ionosonde observations have suggested the irregular plasma density of the bubbles as the main factor causing the spread-F traces in equatorial ionograms [2] and forcing satellite transionospheric signals to fluctuate wildly in phase and amplitude [3,4]. Such degradations may

cause interference, fading in radio frequency communications and disrupting many applications. Therefore, characterizing the ionospheric plasma bubble extensions and temporal evolutions has been the subject of continued study for decades [5–9].

Temporal evolution and spatial development of the plasma bubbles have been studied extensively using different techniques. Several works have conducted an analysis based on ionosondes measurement, such as Rastogi [10] by reporting seasonal variations of Equatorial Spread F, Saito and Maruyama [11] by studying the day-to-day variability of plasma bubbles, and Wang et al. [12] by using concurrent ionosonde observations with other instruments to correlate the occurrence of scintillations with plasma bubbles. Topside sounders and satellite-based measurements, which can be connected to ground-based observations [13], have also been used to map the plasma bubble distributions, such as for mapping the activity [14] and probability [15] of equatorial spread F, to describe the plasma bubbles' morphology [16–18] and specific distributions during storm events [19], and for showing their association with ionospheric irregularities [20] and plasma blobs [21]. Furthermore, radio scintillation measurements enabled the monitoring of plasma bubbles in the level of signal fluctuations [22], which makes it possible to capture the occurrence of plasma bubbles [23] and their signatures [24], even in the Brazilian area [25,26]. Additionally, all-sky optical instruments providing two-dimensional horizontal images have been presented as relevant tools for mapping instantaneous coverage of the plasma bubble structures [27], as well as for capturing climatological occurrences [28], connections with neutral winds [29], and relations with small- and medium-scale structures [30].

Although many techniques have been developed, a major difficulty in characterizing the plasma bubbles remains due to the limitations of the actual instruments for monitoring the plasma depletions in a sufficiently large area. For instance, the frequently used all-sky optical instruments cover approximately 1600 km of airglow measurements, that is, they are restricted to $\sim 15^\circ$ of latitude and longitude in the equatorial region. Such dimensions are sufficiently good to capture the longitudinal variability of the plasma bubbles, which is around 400 km. However, the latitudinal extension of the plasma bubbles can reach distances of 5400 km in the equatorial region, since the geomagnetic conjugate points are located at approximately $\pm 20^\circ$ from the equator. In order to overcome such limitations, recent works have made observations of plasma bubbles over a large area using Total Electron Content (TEC) measurements derived from ground-based global navigation satellite system (GNSS) stations [31,32]. The ground-based GNSS observations using more than 130 receivers over South America are not dependent on weather conditions and were capable of capturing plasma depletions with a sufficient spatial resolution at TEC level. Therefore, simultaneous analysis of airglow and GNSS measurements has been presented as a useful tool to monitor plasma bubble structures in a more detailed form.

Previous works have shown clear evidence of equatorial plasma bubbles at TEC level [31,32] by comparing the airglow images with the Vertical TEC (VTEC) parameter obtained with GNSS observations. However, these VTEC values have intrinsic shortcomings, due to the approximation of the ionosphere as a thin shell with a constant height at about 350–450 km above the Earth's surface. Consequently, the accuracy of the plasma bubble boundary is limited, and the resulting maps are applicable only in analyzing the horizontal distributions. Otherwise, the GNSS signal intersects many altitudes of the ionosphere, by allowing its three-dimensional reconstruction by using tomographic algorithms [33]. The use of tomographic reconstruction techniques for recovering horizontal and vertical distributions of the plasma bubbles is a topic of great interest to the community involved in Space Weather, Spatial Geodesy, and Telecommunications, since much about the plasma bubbles' morphology is not fully understood [34]. For instance, the three-dimensional representations could be a useful tool to describe the horizontal and vertical distribution of the plasma bubbles, as well as to contribute to the explanation of their dynamics and evolution.

An ionospheric tomography method was developed by Prol and Camargo [35], with the main purpose of imaging the ionosphere in the Brazilian region. The experimental results provided good estimations of the critical frequency and TEC when compared to conventional ionospheric models.

A further analysis remained to be carried out in order to verify the efficiency of tomography for imaging the ionospheric dynamics over the region. Considering that the spatial variability and evolution of ionospheric plasma bubble irregularities is a topic of major interest in the Brazilian region [36], we present here the possibilities of a new tomographic method for imaging plasma depletions at electron density level. As a result, we show, for the first time, the efficiency of tomographic reconstruction techniques in detecting plasma bubbles over a systematic analysis of several days, using, as reference, simultaneous observations of all-sky images from 630.0 nm atomic oxygen emission, i.e., OI 630 nm all-sky images. Additionally, since the tomographic reconstruction provides three-dimensional representations, the performance of the tomographic algorithm is investigated for analyzing the plasma bubble vertical structures. In this direction, Section 2 shows the proposed method. Section 3 presents the performance of the proposed method to map the horizontal distributions, and Section 4 shows the possibilities of mapping the vertical distributions. Then, Section 5 presents the conclusions of the tomographic method application to map the equatorial plasma bubbles in the Brazilian scenario.

2. Ionospheric Tomography Method

The mathematical formulation of the tomographic reconstruction method was developed in two stages. The first stage uses the climatological model proposed by Prol et al. [37] to build the background ionosphere based on global Radio-Occultation (RO) observations. The second refers to a slight modification of the Multiplicative Algebraic Reconstruction Technique (MART) for an iterative update of the background electron density field, using regional observations of TEC. Both methods were applied using data spanning over twenty-three days from 2013 and 2014 with clear evidence of plasma bubble structures propagating through the Brazilian region, and the following subsections show the mathematical aspects in details.

2.1. Ionospheric Background

The background ionosphere was developed in terms of a climatological model, using RO ionospheric profiles derived from the Constellation Observing System for Meteorology, Ionosphere, and Climate (COSMIC)/Formosa Satellite Mission 3 (COSMIC/FORMOSAT-3) mission. Six parameters were estimated to describe climatological patterns of the ionospheric profiles: Electron density at the peak (N_m), peak height (h_m), scale height of the topside referred to h_m (H_0), scale height gradient at the topside ($\partial H/\partial h$), thickness of the bottomside (B_0), and scale factor of the bottomside (B_1). The peak parameters h_m and N_m were directly retrieved from ionospheric profiles processed by the University Corporation for Atmospheric Research (UCAR). On the other hand, a least-square fitting was performed by the authors for the topside and bottomside estimation. The following equations were used for the topside:

$$n_e^t = N_m e^{0.5(1-z_t - e^{-z_t})} \quad (1)$$

with:

$$z_t = \frac{h - h_m}{\partial H/\partial h(h - h_m) + H_0} \quad (2)$$

and the following equations for the bottomside:

$$n_e^b = \frac{N_m e^{-(z_b)^{B_1}}}{\cosh(z_b)} \quad (3)$$

being:

$$z_b = \frac{h_m - h}{B_0} \quad (4)$$

where n_e represents the observed electron densities at the height h for the topside (n_e^t) and bottomside (n_e^b).

A thirty-day sliding window using RO measurements was defined for the global representation. A spatial bilinear interpolation was carried out for each parameter (h_m , N_m , H_0 , $\partial H/\partial h$, B_0 , and B_1) in terms of local time (LT) and magnetic latitude. The resulting global maps were converted to the Earth-fixed reference frame by projecting the LT maps along with the geomagnetic lines. As a result, two-dimensional grids (2D) were generated with a spatial resolution of 2° in latitude by 4° in longitude, and a temporal resolution of 6 min in Universal Time (UT). Therefore, it was possible to interpolate h_m , N_m , H_0 , $\partial H/\partial h$, B_0 , and B_1 for a specific regular grid in UT, and then to calculate the electron density at any height in the Brazilian grid in order to create the background for regional tomography.

2.2. Regional Tomography

Once the ionospheric background is calculated, regional tomography is performed using ground-based dual-frequency receivers from the continuously operating GNSS stations throughout South America. We used data from RBMC (Brazilian Network for Continuous GNSS Monitoring), IGS (International GNSS Service), CALIBRA (Countering GNSS high Accuracy applications Limitations due to Ionospheric disturbances in Brazil), LISN (Low latitude Ionospheric Sensor Network), and RAMSAC (Red Argentina de Monitoreo Satelital Continuo) to derive the tomographic images. Figure 1 shows the location of the GNSS stations operating in the Day of Year (DOY) 3 of 2014.

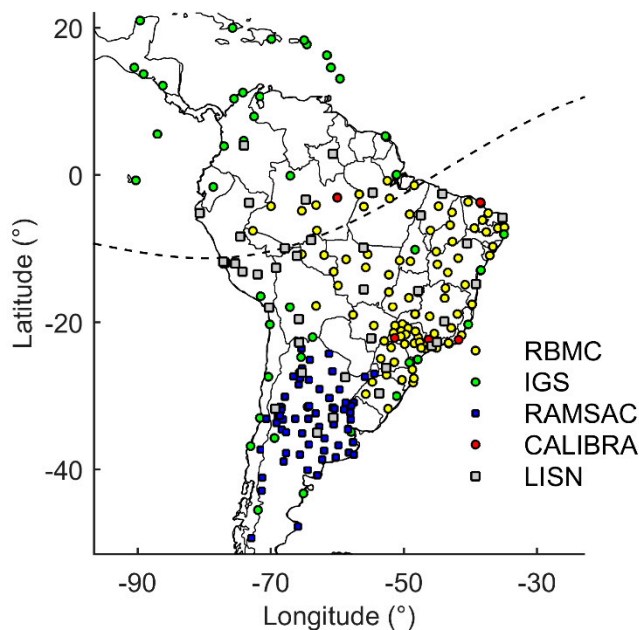


Figure 1. Global navigation satellite system (GNSS) stations operating throughout South America in Day of Year (DOY) 3 of 2014. The colored marks indicate the location of the stations for the different networks, where the dashed line shows the magnetic equator.

Ionospheric tomography was performed using a temporal resolution of 6 minutes and a horizontal resolution of 1° in longitude and 1° in latitude in order to cover the longitudes from 91.5°W to 18°W and the latitudes from 51.5°S to 22°N . The vertical resolution of the 3D grid was constructed with distinct step sizes, varying from 50 km up to 500 km, in order to reduce the number of cells and improve the time process. Each cell of the 3D grid was filled with the initial electron density given by the background. Then, a slightly different method than the conventional MART algorithm was applied in order to iteratively update the initial electron density of each cell j using TEC measurements. The general tomographic system can be expressed as below [38]:

$$\mathbf{y} = \mathbf{A} \mathbf{x} + \boldsymbol{\varepsilon} \quad (5)$$

where \mathbf{y} consists of the TEC measurements, \mathbf{x} is composed by the unknown vector of electron density, A is the design matrix composed by the path length elements of the GNSS signals inside the boundaries of the voxels, and ε stands for the measurement noises and discretization error.

In general, this problem involves many parameters due to the dimensions of the ionosphere. Additionally, the limited number of GNSS viewing angles makes the tomographic inversion an ill-conditioned problem. Therefore, summing up the large dimensions of the matrices and the measurement noise affecting the ill-conditioned system, an iterative process is typically used to perform the estimation procedure. In this regard, the proposed MART algorithm is used with the following equations:

$$x_j^{k+1} = x_j^k \left(\frac{y_i}{A_{ij}, x^k} \right)^{w A_{ij} / A_{max}} \quad (6)$$

and:

$$x_j^{k+2} = x_j^{k+1} \left(\frac{y_i^v}{A_{ij}^v, x^{k+1}} \right)^{w A_{ij}^v / A_{max}^v} \quad (7)$$

where x_j^{k+1} represents the j member of the electron density vector \mathbf{x} at the iteration $k + 1$, A_{ij} is the path length of the GNSS signal i inside the boundaries that intersect cell j , A_{max} is the largest path length of the respective signal i , the inner product A_{ij}, x^k produces the background TEC, w is a weighting parameter that controls the convergence of the algorithm, and y_i and y_i^v are the observed GNSS-based TEC and VTEC, respectively, in which k varies with a stepsize of 2 due to VTEC updates. The iterative process cycles through all ray paths 70 times with a weighting parameter of $w = 0.2$, both parameters being empirically obtained. The slight difference from the conventional MART was defined in this procedure by the incorporation of vertical TEC observations in addition to the slant TEC. In this direction, updates are performed using A_{ij}^v and A_{max}^v as the vertical distance of the path lengths of A_{ij} and A_{max} , respectively.

TEC observations of Equation (5) were obtained with the high precise calibration process developed by Prol et al. [39], and the VTEC observations of Equation (6) were derived by $VTEC_i = TEC_i / M_i$, where M_i stands for the standard mapping function. While the TEC updates correspond to a set of cells in the slant direction of the GNSS signal, the VTEC estimations correspond to the vertical column of voxels above and below the ionospheric pierce point corresponding to the 450 km shell height. This strategy improves the description of the ionospheric horizontal features in regions with lack of slant TEC, without significantly affecting the TEC estimation in regions with a high amount of slant observations. Therefore, the use of both measurements (slant TEC and VTEC) generates a tomographic reconstruction with an increased number of illuminated cells, which is an important aspect for mapping the plasma bubble structures.

3. Horizontal Distribution of Plasma Bubbles

The validation of the tomographic method as a tool to map the horizontal distributions of the plasma bubbles was performed comparing the reconstructed VTEC maps with images derived from all-sky optical instruments. The next subsection demonstrates the feasibility of mapping the horizontal distributions of plasma bubbles through a set of comparative examples between the reconstructed VTEC plasma bubbles with the airglow images. Then, Section 3.2 presents the validation of the proposed method by means of a systematic analysis over several days. For both experiments, three all-sky optical instruments, with 180° wide-angle fisheye lens, were used to detect the red line emission of atomic oxygen at 630 nm in the ionosphere. Two of them are located in the equatorial region, at São João do Cariri (7.4°S, 36.5°W, dip latitude 11.11°S) and Boa Vista (2.8°N, 60.7°W, dip latitude 15.14°N), and the other is located in the southern crest of the Equatorial Ionization Anomaly (EIA), at Cachoeira Paulista (22.7°S, 45.0°W, dip latitude 19.7°S). The OI 630 nm images are freely provided by INPE (Instituto Nacional de Pesquisas Espaciais) and cover a latitudinal extension and a longitudinal extension of 1280 × 1280 km, with a pixel resolution of 2.5 km for the height

of 250 km. The airglow images were recorded with a temporal resolution of six minutes, following the same temporal resolution of the VTEC maps.

3.1. Feasibility of Mapping Plasma Bubbles by the Tomographic Reconstruction

Figure 2 shows an example of the VTEC map retrieved from the tomographic algorithm (left panel) and the corresponding OI 630 nm images (right panel) in DOY 3 of 2014 at 1.9 h UT (Universal Time). Two well-defined VTEC depletions can be seen aligned with the geomagnetic field lines around 21 and 24 h in Local Time (LT), which are also coincident with signatures of the plasma bubble in the airglow images. At such instants, the plasma that was uplifted to higher altitudes, as a result of the post-sunset enhancement in the equatorial $\mathbf{E} \times \mathbf{B}$ drift, increased the growth rate of the spread- F plasma instabilities. Thus, the well-developed large-scale plasma bubble irregularities expanding to higher latitudes generated depletions observed at VTEC level. Since the emission rate of OI 630.0 nm nightglow is primarily a consequence of a charge exchange involving the ion O^+ and O_2 and because there is a lower oxygen density (O_2) at higher altitudes, the elevation of the F layer generates a large region of ionization depletion seen as darkened flux tubes [40]. As expected, we have observed VTEC depletions aligned with a decrease in the intensity of the OI 630 nm images given by the dark brands. Plasma depletions in the VTEC maps were more evident in Cachoeira Paulista (CHPI) and Boa Vista (BOAV) than in São João do Cariri (SJCI). Indeed, SJCI is located at the edge of the reconstructed area, where the geometrical coverage of the GNSS signal is too weak to efficiently perform ionospheric tomography. It is also important to notice that few observations are used in the north-eastern region, above 10°N , and in the eastern side of 50°W . In fact, there are some GNSS signals crossing the topside ionosphere, but few observations near the peak height. The VTEC representation of this part is, therefore, mainly associated to the background model and, as expected, some artifacts are observed in the reconstructed images due to the high TEC variation in the transition between the background and the regional reconstruction.

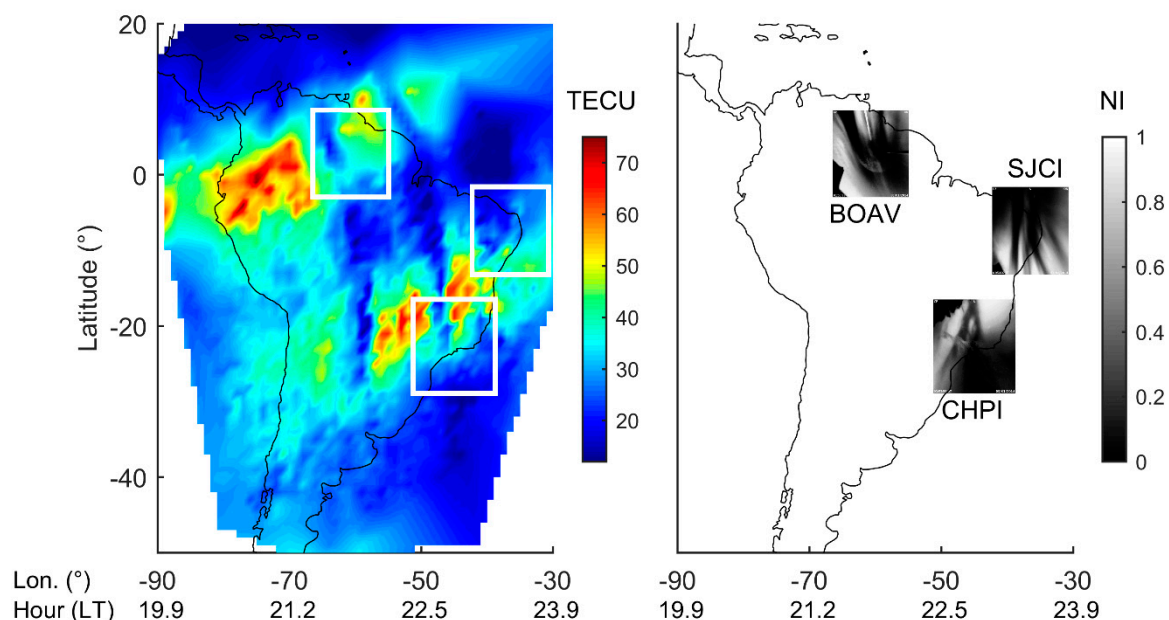


Figure 2. Comparative example between the Vertical Total Electron Content (VTEC) depletions and the dark brands of the airglow observations. The white square shows the exact location of the Geo-referenced OI 630 nm images and the grayscale is in units of normalized intensity (NI).

Although the plasma bubble was not so evident in SJCI at DOY 3/2014, the plasma depletions can be clearly observed in the VTEC maps presented for DOY 359/2013 in Figure 3. It is possible to see the VTEC depletion aligned with the dark brands of the airglow images due to the larger longitudinal

dimensions of the plasma bubble of DOY 359/2013 in comparison with the plasma bubble of DOY 3/2014. Thus, even with problems of coverage in the tomographic reconstruction at SJCI, it is possible to detect plasma bubbles in case the dimensions of the ionospheric structure are large enough to be captured.

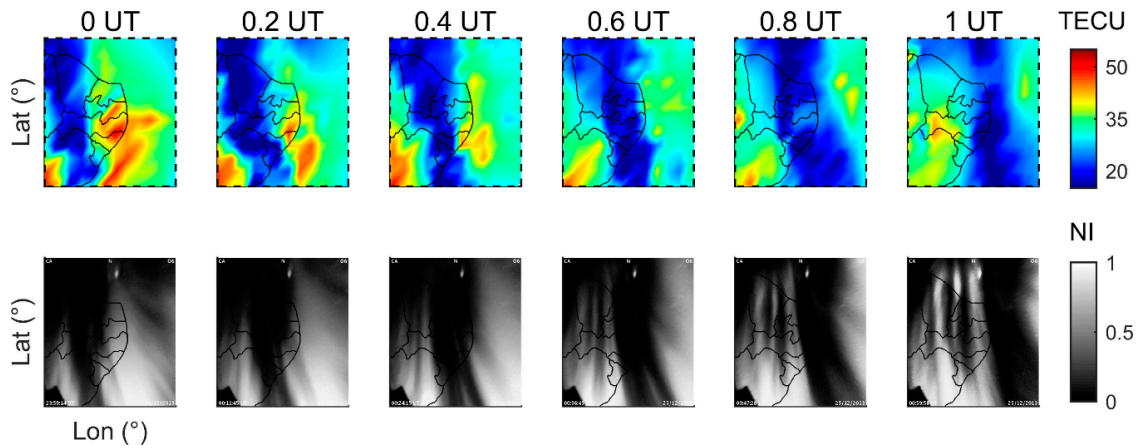


Figure 3. Example of a plasma bubble propagating through São João do Cariri (SJCI) in DOY 359 of 2013, detected by the VTEC reconstructions and the optical instruments.

VTEC depletions are not only observed with a similar location and dimensions to the airglow observations, but they also follow the plasma bubble orientation. For instance, Figure 4 shows that the azimuth of the VTEC depletion mapped in CHPI at DOY 3/2014 is changing accordingly with the azimuth of the airglow dark intensities, which also happened for other instruments and days. In all cases with plasma bubble detections, a longitudinal discrepancy can also be observed between the VTEC depletion and the darker brand of the airglow emissions. A similar discrepancy was observed in [31], which might indicate that the bubble is tilted westward with the increasing height [3,41].

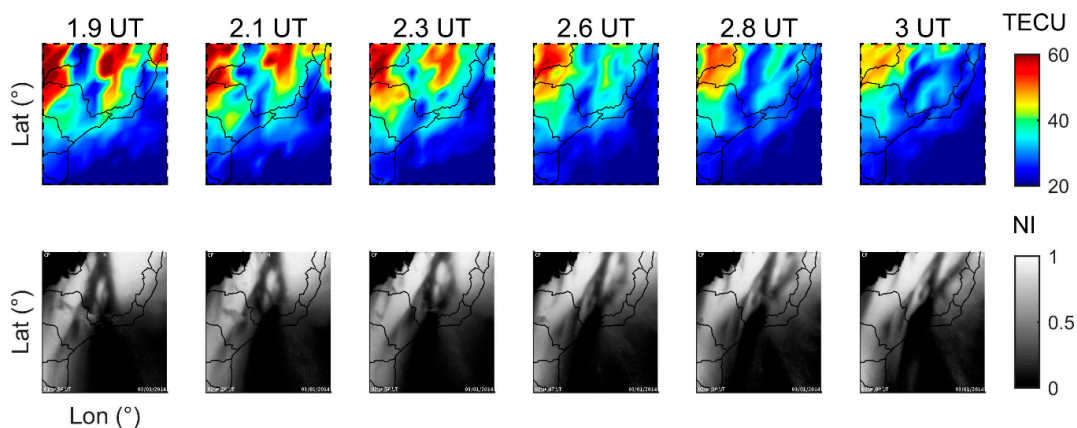


Figure 4. Example of a plasma bubble propagating through Cachoeira Paulista (CHPI) in DOY 3 of 2014 detected by the VTEC reconstructions and the optical instruments.

Additionally, Figure 5 shows a collection of west–east slices of the reconstructed VTEC maps as a form of a keogram. This is presented in order to compare the obtained reconstructions with the keogram presented by Barros et al. [42], which observed equatorial plasma bubbles through a direct interpolation of VTEC values instead of using tomography. The same days and configurations of South America GNSS stations are used here and we are presenting the results for the same 25°S latitudinal section. Considering the zonal velocity as the ratio between $\Delta\text{longitude}/\Delta\text{time}$, we can see three plasma bubble signatures (PB1, PB2, and PB3) in the keogram, with a general motion progressing from

west to east throughout the night. Despite the worse resolution of the tomography in comparison to the keogram presented by Barros et al. [42], the interbubble distances around 600 km and the inclination of the plasma bubble signatures producing a zonal velocity of 160 m/s (PB1), 144 m/s (PB2), and 128 m/s (PB3) are consistent with their results, which confirms the feasibility of the tomographic reconstruction when compared with a robust single-layer interpolation procedure.

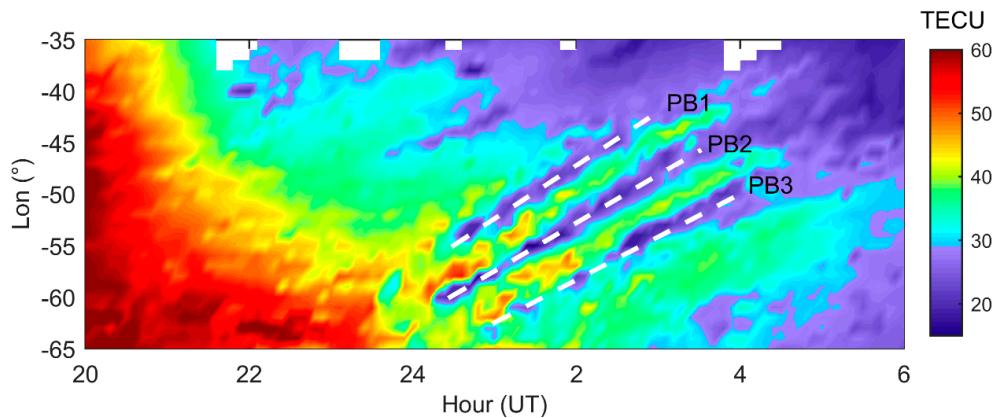


Figure 5. Keogram of the VTEC values at the latitudinal section of 25°S in terms of longitude and hours at the night of DOYs 358 and 359 from 2013.

3.2. Systematic Assessment

In order to give an overview of the efficiency of the tomographic reconstruction for mapping the plasma bubbles, the experimental comparisons of Figures 2–4 were carried out in a systematic analysis over several other events. Twenty-three days were selected during the summer Sun of the solar maximum period of 2013 and 2014, when we found clear evidence of plasma bubbles propagating through the Brazilian region with the optical instruments. The days chosen were DOYs 358–363 of 2013, as well as DOYs 3–6, 8, 9, 11, and 21–30 of 2014. It was possible to analyze the temporal evolution of the VTEC depletions aligned with the signatures of plasma bubbles in the airglow images for many events, and the general rate of success of the tomographic reconstruction was organized in the form of a confusion matrix. The main goal of the confusion matrix was to show the number of detected plasma bubbles with the VTEC and airglow images, as well as the number of non-detected plasma bubbles by each instrument. Since it is sometimes difficult to confirm whether the plasma bubbles were detected, a third piece of information was included in the confusion matrix, named as uncertain bubbles.

The classification of each feature of the confusion matrix was made according to the authors' interpretation, and Figures 6–8 show a few examples of the classification. They show the main classes of the confusion matrix: (a) Images with plasma bubbles mutually detected by the tomographic method and the optical instruments; (b) plasma bubbles detected by the airglow images, but not detected in the VTEC reconstructions; (c) images with detected plasma bubbles at VTEC level, but not detected in the airglow images; and (d) plasma bubbles not detected by any instrument. All of these examples are presented for the observatory of Cachoeira Paulista, in which Case (a) refers to DOY 22 of 2014 at 1.5 UT (22.5 LT at the central longitude), Case (b) to DOY 24 of 2014 at 0.8 UT (21.8 LT at the central longitude), Case (c) to DOY 358 of 2013 at 0.5 UT (21.5 LT at the central longitude), and Case (d) to DOY 360 of 2013 at 0 UT (21 LT at the central longitude).

A detailed inspection of the images was conducted by visual analysis of each VTEC and airglow images. Taking Case (a) as an example, we can clearly see the presence of a plasma depletion at VTEC level of Figure 6, and a simultaneous dark brand in Figure 7. When looking at the entire South America scenario of Figure 8, we then confirm that the correspondent VTEC depletion refers to a large-scale irregularity aligned with the geomagnetic field line. Indeed, Figure 8 is also used in the analysis in order to support the decision, mainly because, sometimes, small-scale irregularities, together with few observations in the reconstructed region, can produce substantial VTEC depletions in the observatories

and lead to an incorrect classification. For instance, Case (b) shows a small VTEC depletion in Figure 6, which could be misinterpreted as the southern region of a plasma bubble. Therefore, when looking at the entire South America region, we confirm the plasma bubbles' absence. It is relevant to say that the color bar limits were changed accordingly for the comparison of each VTEC depletion. The same analysis of the four cases (a, b, c, and d) was conducted by looking image by image with a temporal resolution of 6 minutes for each time airglow observations were collected. In the end, a total of 739, 709, and 610 images were analyzed in CHPI, SJCI, and BOAV, respectively, to cover the twenty-three days, and the results are summarized in three confusion matrices (Tables 1–3).

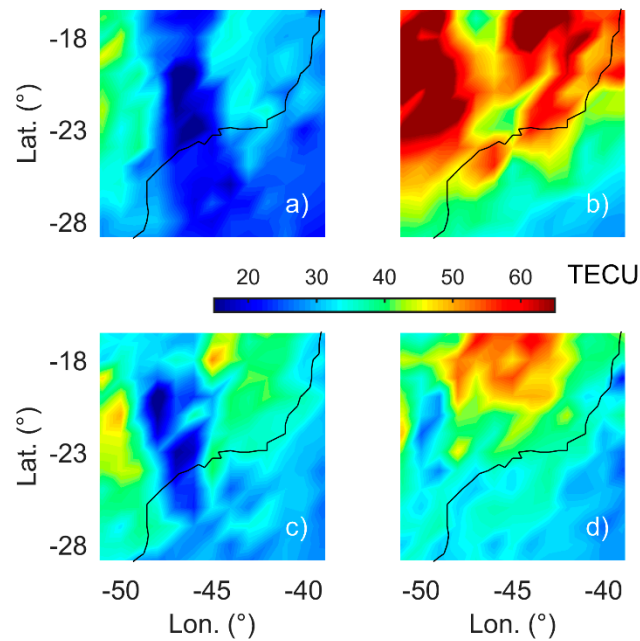


Figure 6. Four cases to build the confusion matrix using the VTEC reconstructions in CHPI.

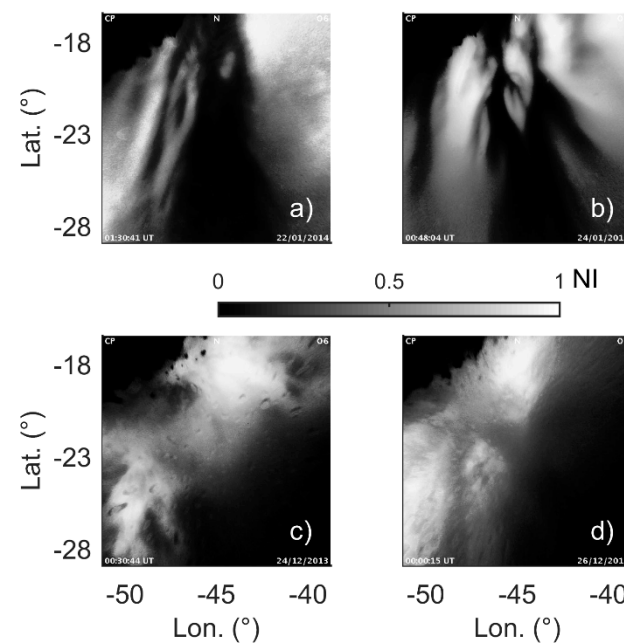


Figure 7. Four cases to build the confusion matrix using the airglow observations in CHPI.

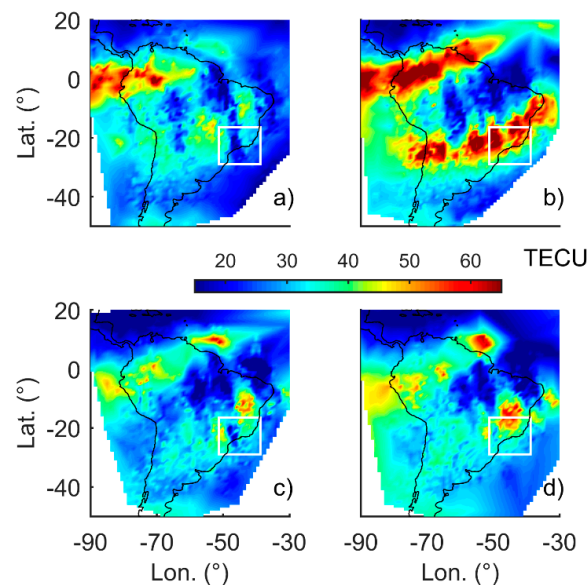


Figure 8. Four cases to build the confusion matrix using the VTEC reconstructions over all the South America region. The white square shows the coverage of the CHPI images.

Table 1 presents the obtained numbers in Boa Vista, where the 1st line and 1st column of the matrix (or Table) refers to the number of images where the plasma bubbles were mutually detected by VTEC and airglow observations. The number 181, for instance, reveals that 181 plasma bubbles were mutually seen by the instruments, which represents 29% of images used in the analysis in Boa Vista. The last position of the matrix (3rd line and 3rd column) shows the number of images without plasma bubbles in any method. The matrix also shows the relevant information of the 1st line and 3rd column, which is that 117 airglow images detected plasma bubbles not seen on the VTEC maps. This is one of the most important features, since it directly shows the errors obtained with the tomographic method in comparison to the airglow images. On the other hand, the 3rd line and 1st column shows that 21 plasma bubbles were detected by the tomographic method, but not captured by the optical instruments. This is also an important point, because it says that the tomographic method is more accurate in some instances, which is likely true due to the meteorological limitations of the airglow emissions.

Table 1. Confusion matrix showing the number and percentage of plasma bubbles detected by the tomographic reconstruction and optical instruments in the observatory of Boa Vista.

		Tomography		
		With Bubbles	Uncertain	Without Bubbles
Airglow	With Bubbles	181 (29%)	36 (5.9%)	117 (19%)
	Uncertain	6 (0.9%)	34 (5.6%)	80 (13%)
	Without Bubbles	21 (3.4%)	0 (0%)	135 (22%)

Table 2. Confusion matrix showing the number and percentage of plasma bubbles detected by the tomographic reconstruction and optical instruments in the observatory of São João do Cariri.

		Tomography		
		With Bubbles	Uncertain	Without Bubbles
Airglow	With Bubbles	133 (18%)	102 (14%)	187 (26%)
	Uncertain	5 (0.7%)	28 (3.9%)	29 (4.1%)
	Without Bubbles	21 (2.9%)	0 (0%)	204 (29%)

Table 3. Confusion matrix showing the number and percentage of plasma bubbles detected by the tomographic reconstruction and optical instruments in the observatory of Cachoeira Paulista.

		Tomography		
		With Bubbles	Uncertain	Without Bubbles
Airglow	With Bubbles	108 (15%)	71 (9.6%)	242 (33%)
	Uncertain	0 (0%)	23 (3.1%)	33 (4.5%)
	Without Bubbles	51 (6.9%)	32 (4.3%)	179 (24%)

An overall analysis of the results given by Tables 1–3 shows that the highest amount of plasma bubbles detected by optical instruments was obtained in CHPI, since there are more airglow data for this station. The rate of success of the tomographic method was defined by taking the ratio of the mutually detected plasma bubbles (1st line and 1st column) from the sum of the amount of plasma bubbles detected only by the optical images (all columns of the 1st line). In this regard, the rate of success of the tomographic method to detect plasma bubbles was 54.2%, 31.5%, and 25.7% for BOAV, SJCI, and CHPI, respectively. Actually, the lowest rate of success in CHPI suggests that the tomographic method is better at lower latitudes, which is expected because the dimensions of the plasma bubbles are larger in such regions. In addition, CHPI is located in the region with the highest ionospheric variability for the analyzed season. On the other hand, the CHPI region presented 51 images with plasma bubbles in the VTEC maps that were not detected by the airglow images. This is mainly due to the meteorological conditions at CHPI, where clouds of precipitation disrupted the plasma bubbles imaging, or even due to moonlight brightness contamination.

The ionospheric irregularity activity in the Brazilian sector is well known to be more intense during the December solstice months (summer), when, for example, there is a close alignment between the sunset terminator and the magnetic meridian in the longitude of CHPI. This enhancement in irregularity activity is a consequence of the strong evening equatorial vertical plasma drifts, which transport plasma to higher latitudes and increase its density around the crests of the EIA. Consequently, during December 2013 and January 2014, the electron density ambient and the plasma density gradients are more intense to produce ionospheric irregularities, with much higher variabilities in the latitude of CHPI, as confirmed by the airglow detections shown in Tables 1–3. However, the high overall level of ionospheric irregularities is responsible for the generation of many ionospheric scintillations in the GNSS signals crossing the CHPI region, which produces GNSS loss of lock and reinitializations of the TEC calculation. As a result, few observations of TEC are used in the tomographic reconstruction of the CHPI region, due to the high instability of the ionospheric irregularities. Therefore, it needs to be considered that plasma bubble detection may become problematic at instances with high TEC variability, which seems contradictory to the main goal of using the GNSS-based tomographic algorithm for mapping plasma bubbles.

4. Vertical Distribution of Plasma Bubbles

This Section shows vertical distributions of the reconstructed ionosphere when applying the proposed tomographic algorithm in instances with evident plasma bubbles. To demonstrate the overall scenario of the reconstructed ionosphere, ionospheric profiles during plasma bubble events were analyzed together with the horizontal distributions. Figure 9 shows VTEC maps obtained at DOY 32 of 2014, and Figure 10 shows the correspondent keogram, where it is possible to see a plasma bubble propagating northeastward with an estimated zonal velocity of 149 m/s. A white line was included in the longitudinal sector of 55°W in order to analyze the vertical distribution at this specific longitude. As can be seen, the plasma bubble becomes noticeable at 0.6 h UT on the left side of the white line, then it becomes more evident at 1 h UT above the line and overpasses the longitudinal sector at 1.8 h UT. The white line is set at 20.7 LT during 0.4 UT and goes up to 22.1 LT at 1.8 UT.

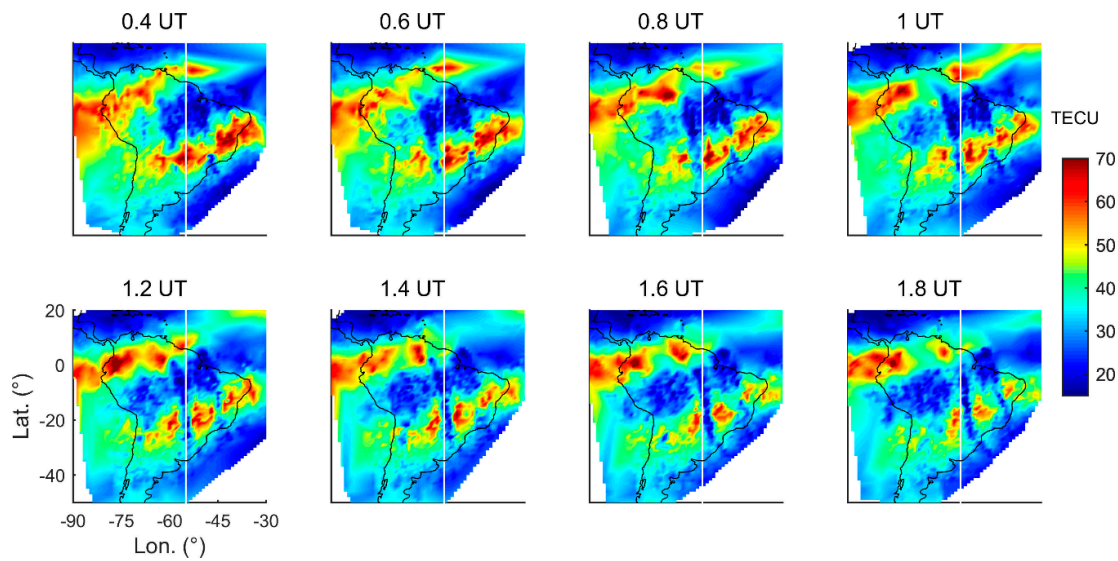


Figure 9. Reconstructed VTEC maps during the propagation of an ionospheric plasma bubble over the South America region. The white line is designed at the longitudinal sector of 55° W.

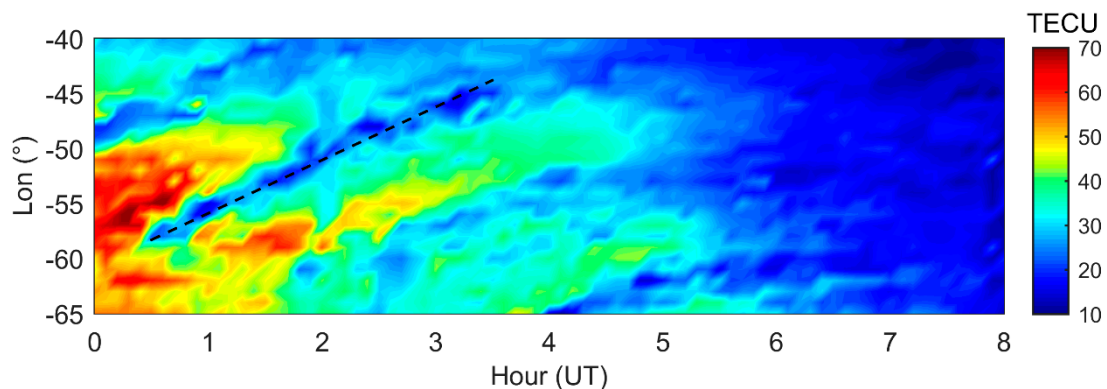


Figure 10. Keogram of VTEC values in terms of longitude and hour at the latitudinal section of 24° S during DOY 32 from 2014.

Figure 11 shows the corresponding vertical images of the longitudinal section given by the white line in order to reproduce the vertical distribution of the scenario presented in Figure 9. The reconstructed tomograms, given in terms of latitude by altitude, are similar to those presented by [43], which analyzed a region of Russia in a bidimensional reconstruction. Now, however, the 3D reconstruction allows us to correlate VTEC images with the tomograms. In general, these Brazilian tomograms present typical representations of the north and south crests of EIA in terms of electron density at 0.4 and 0.6 UT, or 20.7 and 20.9 LT. However, when VTEC depletion reaches the 55° W longitudinal sector at 0.8 hours UT (21.1 LT), the electron density of the south crest of EIA reduces substantially, almost disappearing. In such instances, when the radio-frequency signals overpass the diffraction points of the ionospheric irregularities, destructive and constructive interferences are supposed to cause ionospheric scintillations and spread-F signatures on ionograms. However, after 1.6 h UT (21.9 LT), the south crest of EIA reappears and many ionospheric irregularities dissipate. It is worth mentioning that this event was better characterized in the south crest than the north crest, due to the higher amount of GNSS data in the south region.

It is well known that vertical representations of ionospheric tomography are highly dependent on the background [44]. Therefore, the intrinsic limitations of ionospheric tomography for the height estimation suggest that the ionospheric irregularities presented in Figure 11 could be at higher or lower altitudes. Additionally, it is typically observed that the electric field in the region of the structure creates

bifurcations in the plasma bubbles as it extends towards to higher latitudes. However, this effect is not reproduced due to the weak geometry of the GNSS signals for tomographic applications. However, despite the problems in correctly mapping the vertical altitudes of the irregularities and bifurcations, the 3D tomographic reconstruction shows a strong potential to analyze the general vertical distribution of ionospheric irregularities, which indicates future possibilities of building ionospheric models to describe the three-dimensional impact of ionospheric irregularities on the transionospheric signals.

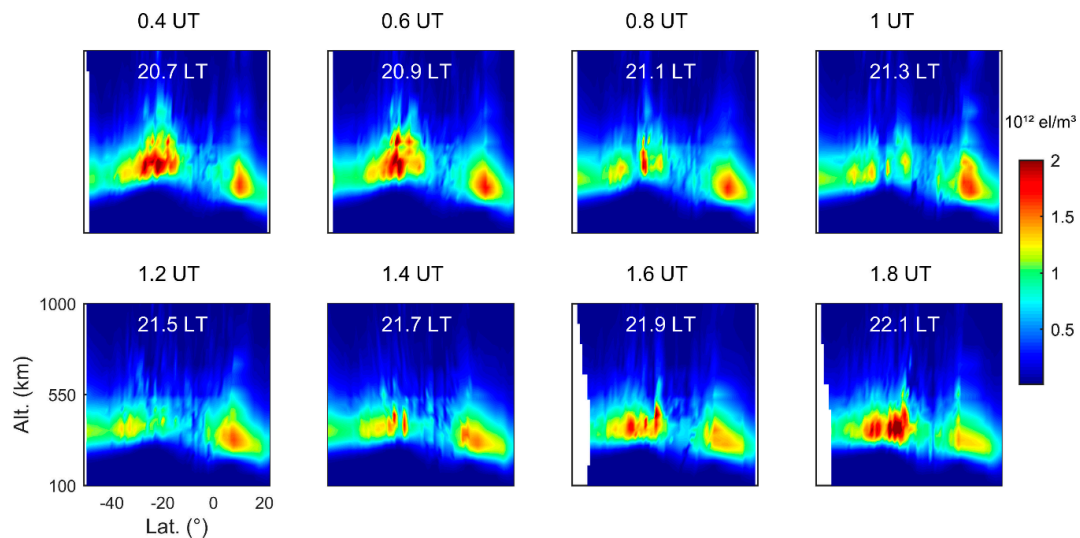


Figure 11. Reconstructed ionospheric profiles during the propagation of an ionospheric plasma bubble over the longitudinal sector of 55°W.

5. Conclusions

A new tomographic reconstruction technique was successfully implemented for imaging the spatial distribution of ionospheric plasma bubbles in the Brazilian region. The mapped horizontal distributions of VTEC depletions were simultaneously compared to the darker bands observed by all-sky airglow imagers in the OI 630 nm emissions. A systematic analysis using 23 days in the peak of the solar cycle 24 was carried out and revealed the rate of success of the tomographic method of 54.2%, 31.5%, and 25.7% for observatories in Boa Vista, São João do Cariri, and Cachoeira Paulista, respectively. The results suggest that the tomographic method is more efficient in the equatorial region, which is expected due to the larger dimensions of the plasma bubbles near the magnetic equator and the higher ionospheric variability in the crests of EIA. However, despite the problems of imaging plasma bubbles with tomographic reconstructions, the latitudes of the VTEC maps covered more than 30° of the plasma bubbles structures and have detected the depletion structures at instances where the meteorological conditions disrupted the possibility of analyzing the OI 630 nm emissions with optical instruments. Additionally, the tomographic reconstructions have shown how the vertical structure of the plasma bubbles can be estimated, which can be useful for further description of the impact of 3D ionospheric irregularities on the transionospheric signals. In future, two analyses are suggested: (1) To validate the plasma bubble vertical reconstruction using the ionosonde data as reference; and (2) to use an accurate method to perform the GNSS-TEC estimation using only single-frequency L1 data. This way, it is expected that fewer TEC gaps will be obtained for plasma bubble imaging, mainly during scintillation events, since the tomographic reconstruction will likely be less sensitive to loss of locks than using dual-frequency TEC estimations.

Author Contributions: This research was performed by F.S.P.; supervised by P.d.O.C.; M.T.d.A.H.M.; and M.H.-P. These authors contributed extensively and equally to prepare this paper.

Funding: This work was jointly funded by Coordenação de Aperfeiçoamento de Pessoal de Nível Superior (CAPES), Fundação de Amparo à Pesquisa do Estado de São Paulo (FAPESP Grants: 2015/15027-7

and 2016/22011-2), and Conselho Nacional de Desenvolvimento Científico e Tecnológico (CNPq Grants: 304674/2014-1, 429885/2016-4 and 309832/2016-0).

Acknowledgments: The authors are grateful to UCAR (USA) and NSPO (Taiwan) for providing COSMIC/FORMOSAT-3 RO data and to IGS, IBGE, INPE, CALIBRA project, LISN project, and the Instituto Geográfico Nacional of Argentina for providing ground-based GNSS data.

Conflicts of Interest: The authors declare no conflict of interest.

References

1. Abdu, M.A. Equatorial ionosphere–thermosphere system: Electrodynamics and irregularities. *Adv. Space Res.* **2005**, *35*, 771–787. [[CrossRef](#)]
2. Lee, C.-C.; Su, S.-Y.; Reinisch, B.W. Concurrent study of bottomside spread F and plasma bubble events in the equatorial ionosphere during solar maximum using digisonde and ROCSAT-1. *Ann. Geophys.* **2005**, *23*, 3473–3480. [[CrossRef](#)]
3. Haase, J.S.; Dautermann, T.; Taylor, M.J.; Chapagain, N.; Calais, E.; Pautet, D. Propagation of plasma bubbles observed in Brazil from GPS and airglow data. *Adv. Space Res.* **2011**, *47*, 1758–1776. [[CrossRef](#)]
4. Paznukhov, V.V.; Carrano, C.S.; Doherty, P.H.; Groves, K.M.; Caton, R.G.; Valladares, C.E.; Seemala, G.K.; Bridgwood, C.T.; Adeniyi, J.; Amaeshi, L.L.N.; et al. Equatorial plasma bubbles and L-band scintillations in Africa during solar minimum. *Ann. Geophys.* **2012**, *30*, 675–682. [[CrossRef](#)]
5. Singh, S.; Bamgboye, D.K.; McClure, J.P.; Johnson, F.S. Morphology of equatorial plasma bubbles. *J. Geophys. Res.* **1997**, *102*, 20019–20029. [[CrossRef](#)]
6. Burke, W.J.; Gentile, L.C.; Huang, C.Y.; Valladares, C.E.; Su, S.Y. Longitudinal variability of equatorial plasma bubbles observed by DMSP and ROCSAT-1. *J. Geophys. Res. Space Phys.* **2004**, *109*, A12301. [[CrossRef](#)]
7. Nishioka, M.; Saito, A.; Tsugawa, T. Occurrence characteristics of plasma bubble derived from global ground-based GPS receiver networks. *J. Geophys. Res.* **2008**, *113*, A05301. [[CrossRef](#)]
8. Patel, K.; Singh, A.K. Characteristic of plasma bubbles observed by DMSP in the topside ionosphere during the year 2005. *J. Earth Syst. Sci.* **2010**, *119*, 211–220. [[CrossRef](#)]
9. Xiong, C.; Lühr, H.; Ma, S.Y.; Stolle, C.; Fejer, B.G. Features of highly structured equatorial plasma irregularities deduced from CHAMP observations. *Ann. Geophys.* **2012**, *30*, 1259–1269. [[CrossRef](#)]
10. Rastogi, R.G. Seasonal variation of equatorial spread F in the American and Indian zones. *J. Geophys. Res.* **1980**, *85*, 722–726. [[CrossRef](#)]
11. Saito, S.; Maruyama, T. Ionospheric height variations observed by ionosondes along magnetic meridian and plasma bubble onsets. *Ann. Geophys.* **2006**, *24*, 2991–2996. [[CrossRef](#)]
12. Wang, G.J.; Shi, J.K.; Reinisch, B.W.; Wang, X.; Wang, Z. Ionospheric plasma bubbles observed concurrently by multi-instruments over low-latitude station Hainan. *J. Geophys. Res. Space Phys.* **2015**, *120*, 2288–2298. [[CrossRef](#)]
13. Kelley, M.C.; Makela, J.J.; Paxton, L.J.; Kamalabadi, F.; Comberiate, J.M.; Kil, H. The first coordinated ground-based and space-based optical observations of equatorial plasma bubbles. *Geophys. Res. Lett.* **2003**, *30*, 1766. [[CrossRef](#)]
14. Maruyama, T.; Matuura, N. Longitudinal variability of annual changes in activity of equatorial spread F and plasma bubbles. *J. Geophys. Res.* **1984**, *89*, 10903–10912. [[CrossRef](#)]
15. Huang, C.-S.; La Beaujardiere, O.; Roddy, P.A.; Hunton, D.E.; Liu, J.Y.; Chen, S.P. Occurrence probability and amplitude of equatorial ionospheric irregularities associated with plasma bubbles during low and moderate solar activities (2008–2012). *J. Geophys. Res. Space Phys.* **2014**, *119*, 1186–1199. [[CrossRef](#)]
16. Huang, C.Y.; Burke, W.J.; Machuzak, J.S.; Gentile, L.C.; Sultan, P. DMSP observations of equatorial plasma bubbles in the topside ionosphere near solar maximum. *J. Geophys. Res.* **2001**, *106*, 8131–8142. [[CrossRef](#)]
17. Dyson, P.L.; Benson, R.F. Topside sounder observations of equatorial bubbles. *Geophys. Res. Lett.* **1978**, *5*, 795–798. [[CrossRef](#)]
18. Kumar, S. Morphology of equatorial plasma bubbles during low and high solar activity years over Indian sector. *Astrophys. Space Sci.* **2017**, *362*, 93. [[CrossRef](#)]
19. Li, G.; Ning, B.; Zhao, B.; Liu, L.; Wan, W.; Ding, F.; Xu, J.S.; Liu, J.Y.; Yumoto, K. Characterizing the 10 November 2004 storm-time middle-latitude plasma bubble event in Southeast Asia using multi-instrument observations. *J. Geophys. Res.* **2009**, *114*, A07304. [[CrossRef](#)]

20. Zakharenkova, I.; Astafyeva, E. Topside ionospheric irregularities as seen from multisatellite observations. *J. Geophys. Res. Space Phys.* **2015**, *120*, 807–824. [[CrossRef](#)]
21. Park, J.; Min, K.W.; Lee, J.-J.; Kil, H.; Kim, V.P.; Kim, H.-J.; Lee, E.; Lee, D.Y. Plasma blob events observed by KOMPSAT-1 and DMSP F15 in the low latitude nighttime upper ionosphere. *Geophys. Res. Lett.* **2003**, *30*, 2114. [[CrossRef](#)]
22. Basu, S.; Basu, S. Equatorial scintillations: Advances since ISEA-6. *J. Atmos. Terr. Phys.* **1985**, *47*, 753–768. [[CrossRef](#)]
23. Aarons, J. The longitudinal morphology of equatorial F-layer irregularities relevant to their occurrence. *Space Sci. Rev.* **1993**, *63*, 209–243. [[CrossRef](#)]
24. McNamara, L.F.; Caton, R.G.; Parris, R.T.; Pedersen, T.R.; Thompson, D.C.; Wiens, K.C.; Groves, K.M. Signatures of equatorial plasma bubbles in VHF satellite scintillations and equatorial ionograms. *Radio Sci.* **2013**, *48*, 89–101. [[CrossRef](#)]
25. Rezende, L.F.C.; de Paula, E.R.; Kantor, I.J.; Kintner, P.M. Mapping and Survey of Plasma Bubbles over Brazilian Territory. *J. Navig.* **2007**, *60*, 69–81. [[CrossRef](#)]
26. Muella, M.T.A.H.; Duarte-Silva, M.H.; Moraes, A.O.; de Paula, E.R.; Rezende, L.F.C.; Alfonsi, L.; Affonso, B.J. Climatology and modeling of ionospheric scintillations and irregularity zonal drifts at the equatorial anomaly crest region. *Ann. Geophys.* **2017**, *35*, 1201–1218. [[CrossRef](#)]
27. Shiokawa, K.; Otsuka, Y.; Lynn, K.J.W.; Wilkinson, P.; Tsugawa, T. Airglow-imaging observation of plasma bubble disappearance at geomagnetically conjugate points. *Earth Planets Space* **2015**, *67*, 43. [[CrossRef](#)]
28. Sobral, J.H.A.; Abdu, M.A.; Takahashi, H.; Taylor, M.J.; de Paula, E.R.; Zamlutti, C.J.; Aquino, M.G.; Borba, G.L. Ionospheric plasma bubble climatology over Brazil based on 22 years (1977–1998) of airglow observations. *J. Atmos. Sol. Terr. Phys.* **2002**, *64*, 1517–1524. [[CrossRef](#)]
29. Fukushima, D.; Shiokawa, K.; Otsuka, Y.; Nishioka, M.; Kubota, M.; Tsugawa, T.; Nagatsuma, T.; Komonjinda, S.; Yatini, C.Y. Geomagnetically conjugate observation of plasma bubbles and thermospheric neutral winds at low latitudes. *J. Geophys. Res. Space Phys.* **2015**, *120*, 2222–2231. [[CrossRef](#)]
30. Ogawa, T.; Sagawa, E.; Otsuka, Y.; Shiokawa, K.; Immel, T.I.; Mende, S.B.; Wilkinson, P. Simultaneous ground- and satellite-based airglow observations of geomagnetic conjugate plasma bubbles in the equatorial anomaly. *Earth Planets Space* **2005**, *57*, 385–392. [[CrossRef](#)]
31. Takahashi, H.; Wrasse, C.M.; Otsuka, Y.; Ivo, A.; Gomes, V.; Paulino, I.; Medeiros, A.F.; Denardini, C.M.; Sant’anna, N.; Shiokawa, K. Plasma bubble monitoring by TEC map and 630 nm airglow image. *J. Atmos. Sol. Terr. Phys.* **2015**, *130*, 151–158. [[CrossRef](#)]
32. Takahashi, H.; Wrasse, C.M.; Denardini, C.M.; Pádua, M.B.; de Paula, E.R.; Costa, S.M.A.; Otsuka, Y.; Shiokawa, K.; Monico, J.F.G.; Ivo, A.; et al. Ionospheric TEC Weather Map Over South America. *Space Weather* **2016**, *14*, 937–949. [[CrossRef](#)]
33. Bust, G.S.; Mitchell, C.N. History, current state, and future directions of ionospheric imaging. *Rev. Geophys.* **2008**, *46*, RG1003. [[CrossRef](#)]
34. Retterer, J.M.; Roddy, P. Faith in a seed: On the origins of equatorial plasma bubbles. *Ann. Geophys.* **2014**, *32*, 485–498. [[CrossRef](#)]
35. Prol, F.S.; Camargo, P.O. Ionospheric tomography using GNSS: Multiplicative algebraic reconstruction technique applied to the area of Brazil. *GPS Solut.* **2016**, *20*, 807–814. [[CrossRef](#)]
36. Moraes, A.O.; Vani, B.C.; Costa, E.; Abdu, M.A.; de Paula, E.R.; Sousasantos, J.; Monico, J.F.G.; Forte, B.; Negreti, P.M.S.; Shimabukuro, M.H. GPS availability and positioning issues when the signal paths are aligned with ionospheric plasma bubbles. *GPS Solut.* **2018**, *22*, 95. [[CrossRef](#)]
37. Prol, F.S.; Hernández-Pajares, M.; Camargo, P.O.; Muella, M.T.A.H. Spatial and temporal features of the topside ionospheric electron density by a new model based on GPS radio occultation data. *J. Geophys. Res. Space Phys.* **2018**, *123*, 2104–2115. [[CrossRef](#)]
38. Jin, S.; Li, D. 3-D ionospheric tomography from dense GNSS observations based on an improved two-step iterative algorithm. *Adv. Space Res.* **2018**, *62*, 809–820. [[CrossRef](#)]
39. Prol, F.S.; Camargo, P.O.; Monico, J.F.G.; Muella, M.T.A.H. Assessment of a TEC calibration procedure by single-frequency PPP. *GPS Solut.* **2018**, *22*, 35. [[CrossRef](#)]
40. Pimenta, A.A.; Sahai, Y.; Bittencourt, J.A.; Rich, F.J. Ionospheric plasma blobs observed by OI 630 nm all-sky imaging in the Brazilian tropical sector during the major geomagnetic storm of April 6–7, 2000. *Geophys. Res. Lett.* **2007**, *34*, L02820. [[CrossRef](#)]

41. Makela, J.J.; Kelley, M.C. Field-aligned 777.4-nm composite airglow images of equatorial plasma depletions. *Geophys. Res. Lett.* **2003**, *30*, 1442. [[CrossRef](#)]
42. Barros, D.; Takahashi, H.; Wrasse, C.M.; Figueiredo, C.A.O.B. Characteristics of equatorial plasma bubbles observed by TEC map based on ground-based GNSS receivers over South America. *Ann. Geophys.* **2018**, *36*, 91–100. [[CrossRef](#)]
43. Kunitsyn, V.E.; Andreeva, E.S.; Tereshchenko, E.D.; Khudukon, B.Z.; Nygren, T. Investigations of the ionosphere by satellite radiotomography. *Int. J. Imaging Syst. Technol.* **1994**, *5*, 112–127. [[CrossRef](#)]
44. Prol, F.S.; Camargo, P.O.; Muella, M.T.A.H. Numerical Simulations to Assess ART and MART Performance for Ionospheric Tomography of Chapman Profiles. *Anais da Academia Brasileira de Ciências* **2017**, *89*, 1531–1542. [[CrossRef](#)] [[PubMed](#)]



© 2018 by the authors. Licensee MDPI, Basel, Switzerland. This article is an open access article distributed under the terms and conditions of the Creative Commons Attribution (CC BY) license (<http://creativecommons.org/licenses/by/4.0/>).